

Phase diagrams of Janus fluids with up-down constrained orientations

Riccardo Fantoni,^{1, a)} Achille Giacometti,^{1, b)} Miguel Ángel G. Maestre,^{2, c)} and Andrés Santos^{2, d)}

¹⁾ *Dipartimento di Scienze dei Materiali e Nanosistemi, Università Ca' Foscari Venezia, Calle Larga S. Marta DD2137, I-30123 Venezia, Italy*

²⁾ *Departamento de Física, Universidad de Extremadura, E-06071 Badajoz, Spain*

(Dated: 12 November 2013)

A class of binary mixtures of Janus fluids formed by colloidal spheres with the hydrophobic hemispheres constrained to point either up or down are studied by means of Gibbs ensemble Monte Carlo simulations and simple analytical approximations. These fluids can be experimentally realized by the application of an external static electrical field. The gas-liquid and demixing phase transitions in five specific models with different patch-patch affinities are analyzed. It is found that a gas-liquid transition is present in all the models, even if only one of the four possible patch-patch interactions is attractive. Moreover, provided the attraction between like particles is stronger than between unlike particles, the system demixes into two subsystems with different composition at sufficiently low temperatures and high densities.

I. INTRODUCTION

Engineering new materials through direct self-assembly processes has recently become a new concrete possibility due to the remarkable developments in the synthesis of patchy colloids with different shapes and functionalities. Nowadays, both the synthesis and the aggregation process of patchy colloids can be experimentally controlled with a precision and reliability that were not possible until a few years ago.^{1–5}

Within the general class of patchy colloids, a particularly interesting case is provided by the so-called Janus fluid, where the surface of the colloidal particle is evenly partitioned between the hydrophobic and the hydrophilic moieties, so that attraction between two spheres is possible only if both hydrophobic patches are facing one another.⁶ Several experimental and theoretical studies have illustrated the remarkable properties of this paradigmatic case.^{7,8}

The behavior of patchy particles under external fields has received recent attention.^{9,10} By applying an external electrical or magnetic field, appropriately synthesized dipolar Janus particles may be made to align orientationally, so as to expose their functionally active hemisphere either all up or all down (See Ref. 9, Secs. 1.4.3.1 and 1.4.3.2, and references therein). By mixing the two species one could have in the laboratory a binary mixture of Janus particles where the functionally active patch points in opposite directions for each species.

While theoretical studies have been keeping up with, and sometimes even anticipated, experimental developments, the complexities of the anisotropic interactions in patchy colloids have mainly restricted these investigations to numerical simulations, which have revealed interesting specificities in the corresponding phase diagrams.

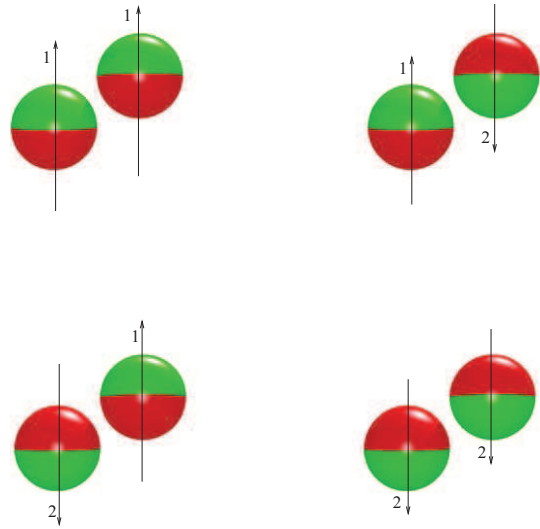


FIG. 1. Sketch of a binary-mixture Janus fluid with up-down constrained orientations. The energy scales of the attractive interactions are (from left to right and from top to bottom) ϵ_{11} , ϵ_{12} , ϵ_{21} , and $\epsilon_{22} = \epsilon_{11}$, respectively. Here we have adopted the convention that ϵ_{ij} is the energy scale when a particle of species i is “below” a particle of species j .

Motivated by the above scenario, we have recently introduced a simplified binary-mixture model of a fluid of Janus spheres (interacting via the anisotropic Kern–Frenkel potential),¹¹ where the hydrophobic patches on each sphere could point only either up (species 1) or down (species 2).¹² This orientational restriction, which is reminiscent of Zwanzig’s model for liquid crystals, clearly simplifies the theoretical description while still distilling out the main features of the original Janus model.

In the present paper, we generalize the above Janus fluid model by assuming arbitrary values for the energy scales ϵ_{ij} of the attractive interactions associated with the four possible pair configurations (see Fig. 1), which allows for a free tuning of the strength of the patch-patch attraction. In some cases this can effectively mimic the

^{a)} Electronic mail: rfantoni@ts.infn.it

^{b)} Electronic mail: achille.giacometti@unive.it

^{c)} Electronic mail: maestre@unex.es

^{d)} Electronic mail: andres@unex.es;
<http://www.unex.es/eweb/fisteur/andres>

reduction of the coverage in the original Kern–Frenkel model. Note that, in Fig. 1, ϵ_{ij} is the energy associated with the (attractive) interaction between a particle of species i (at the left) and a particle of species j (at the right) when the former is below the latter, with the arrow always indicating the hydrophobic (i.e. attractive) patch. The original Kern–Frenkel model then corresponds to $\epsilon_{12} > 0$ and $\epsilon_{11} = \epsilon_{22} = \epsilon_{21} = 0$, whereas the full coverage limit is equivalent to $\epsilon_{11} = \epsilon_{22} = \epsilon_{12} = \epsilon_{21} > 0$. On the other hand, the effect of reducing the coverage from the full to the Janus limit, can be effectively mimicked by fixing $\epsilon_{12} > 0$ and progressively decreasing ϵ_{21} and $\epsilon_{11} = \epsilon_{22}$. Moreover, the class of models depicted in Fig. 1 allows for an interpretation more general and flexible than the hydrophobic-hydrophilic one. For instance, one may assume that attraction is only possible when patches of *different* type are facing one another (i.e., $\epsilon_{11} = \epsilon_{22} > 0$ and $\epsilon_{12} = \epsilon_{21} = 0$). As shown below, this will provide a rich scenario of intermediate cases with a number of interesting features in the phase diagram of both the gas-liquid and the demixing transitions.

We emphasize the fact that in the simulation part of the present study we will always assume “global” equimolarity, that is, the combined number of particles of species 1 (N_1) is always equal to the combined number of particles of species 2 (N_2), so that $N_1 = N_2 = N/2$, where N is the total number of particles. On the other hand, the equimolarity condition is not imposed on each coexisting phase.

The organization of the paper is as follows. The class of models is briefly described in Sec. II. Next, in Sec. III we present our Gibbs ensemble Monte Carlo (GEMC) results for the gas-liquid and demixing transitions. The complementary theoretical approach is presented in Sec. IV. The paper is closed with some concluding remarks in Sec. V.

II. DESCRIPTION OF THE MODELS

In our class of binary-mixture Janus models, particles of species 1 (with a mole fraction x_1) and 2 (with a mole fraction $x_2 = 1 - x_1$) are dressed with two up-down hemispheres with different attraction properties, as sketched in Fig. 1. The pair potential between a particle of species i at \mathbf{r}_1 and a particle of species j at \mathbf{r}_2 is

$$\phi_{ij}(\mathbf{r}_{12}) = \varphi_{ij}(r_{12})\Theta(z_{12}) + \varphi_{ji}(r_{12})\Theta(-z_{12}), \quad (1)$$

where $\Theta(z)$ is the Heaviside step function, $\mathbf{r}_{12} = \mathbf{r}_2 - \mathbf{r}_1$, $z_{12} = z_2 - z_1$, and

$$\varphi_{ij}(r) = \begin{cases} \infty, & 0 \leq r < \sigma, \\ -\epsilon_{ij}, & \sigma \leq r < \sigma + \Delta, \\ 0, & \sigma + \Delta \leq r, \end{cases} \quad (2)$$

is a standard square-well (SW) potential of diameter σ , width Δ , and energy depth ϵ_{ij} , except that, in general,

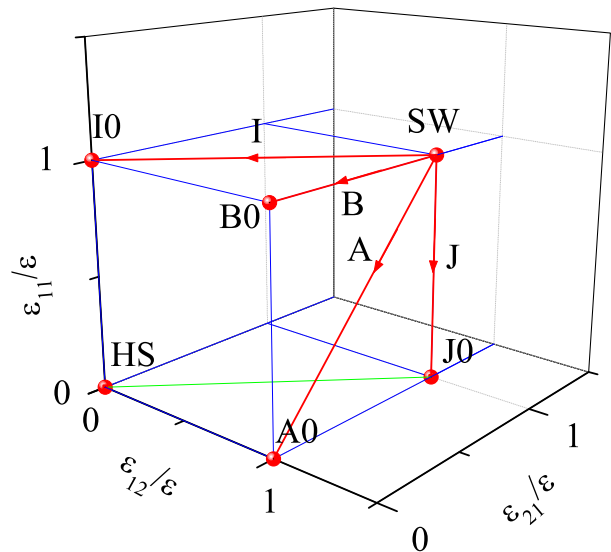


FIG. 2. Parameter space of the class of Janus models defined in the paper.

TABLE I. Definition of the models.

Model	ϵ_{11}	ϵ_{12}	ϵ_{21}	ϵ_{22}
HS	0	0	0	0
A0	0	ϵ	0	0
I0	ϵ	0	0	ϵ
J0	0	ϵ	ϵ	0
B0	ϵ	ϵ	0	ϵ
SW	ϵ	ϵ	ϵ	ϵ

$\epsilon_{12} \neq \epsilon_{21}$. By symmetry, one must have $\epsilon_{22} = \epsilon_{11}$ (see Fig. 1), so that (for given values of σ and Δ) the space parameter of the interaction potential becomes three-dimensional, as displayed in Fig. 2. Except in the case of the hard-sphere (HS) model ($\epsilon_{ij} = 0$), one can freely choose one of the non-zero ϵ_{ij} to fix the energy scale. Thus, we call $\epsilon = \max_{i,j} \{\epsilon_{ij}\}$ and use the three independent ratios ϵ_{ij}/ϵ as axes in Fig. 2. The model represented by the coordinates (1, 1, 1) is the fully isotropic SW fluid, where species 1 and 2 become indistinguishable. Next, without loss of generality, we choose $\epsilon_{12} \geq \epsilon_{21}$. With those criteria, all possible models of the class lie either inside the triangle SW-I0-B0-SW or inside the square SW-B0-A0-J0-SW. One could argue that any point *inside* the cube displayed in Fig. 2 may represent a distinct model, but this is not so. First, the choice $\epsilon = \max_{i,j} \{\epsilon_{ij}\}$ restricts the models to those lying on one of the three faces $\epsilon_{11}/\epsilon = 1$, $\epsilon_{12}/\epsilon = 1$, or $\epsilon_{21}/\epsilon = 1$. Second, the choice $\epsilon_{12} \geq \epsilon_{21}$ reduces the face $\epsilon_{21}/\epsilon = 1$ to the line SW-J0 and the face $\epsilon_{11}/\epsilon = 1$ to the half-face SW-I0-B0-SW. The vertices SW, I0, B0, A0, and J0 define the five distinguished models we will specifically study. Those models, together with the HS one, are summarized in Table I.

The rationale behind our nomenclature for the models goes as follows. Models with $\epsilon_{12} = \epsilon_{21}$ are isotropic and so we use the letter I to denote the isotropic models with $0 \leq \epsilon_{12}/\epsilon = \epsilon_{21}/\epsilon \leq 1$ and $\epsilon_{11}/\epsilon = 1$. Apart from them, the only additional isotropic models are those with $\epsilon_{12}/\epsilon = \epsilon_{21}/\epsilon = 1$ and $0 \leq \epsilon_{11}/\epsilon \leq 1$, and we denote them with the letter (J) next to I. All the remaining models are anisotropic (i.e., $\epsilon_{12} \neq \epsilon_{21}$). Out of them, we use the letter A to denote the particular subclass of anisotropic models ($0 \leq \epsilon_{11}/\epsilon = \epsilon_{21}/\epsilon \leq 1$ and $\epsilon_{12}/\epsilon = 1$) which can be viewed as the anisotropic counterpart of the isotropic subclass I. Analogously, we employ the letter (B) next to A to refer to the anisotropic counterpart ($\epsilon_{11}/\epsilon = \epsilon_{12}/\epsilon = 1$ and $0 \leq \epsilon_{21}/\epsilon \leq 1$) of the isotropic models J. Finally, the number 0 is used to emphasize that the corresponding models are the extreme cases of the subclasses I, J, A, and B, respectively.

Model A0 is the one more directly related to the original Kern–Frenkel potential and was the one analyzed in Ref. 12. Also related to that potential is model B0, where only the interaction between the two hydrophilic patches is purely repulsive. On the other hand, in models I0 and J0 (where $\epsilon_{12} = \epsilon_{21}$) the interaction becomes isotropic and the Janus character of the model is blurred. In model I0 the fluid reduces to a binary mixture with attractive interactions between like components and HS repulsions between unlike ones. This model was previously studied by Zaccarelli et al.¹³ using integral equation techniques. In the complementary model J0 attraction exists only between unlike particles. The points A0, B0, I0, and J0 can be reached from the one-component SW fluid along models represented by the lines A, B, I, and J, respectively. Of course, other intermediate models are possible inside the triangle SW-I0-B0-SW or inside the square SW-B0-A0-J0-SW.

In addition to the energy parameters ϵ_{ij} , the number density ρ , and the temperature T , each particular system is specified by the mixture composition (i.e., the mole fraction x_1). In fact, in Ref. 12 the thermodynamic and structural properties of model A0 were studied both under equimolar and non-equimolar conditions.

III. GIBBS ENSEMBLE MONTE CARLO SIMULATIONS

In this paper, we use GEMC techniques^{14–16} to study the gas-liquid condensation process of models SW, A0, B0, I0, and J0 and the demixing transition of models I0 and B0. We have chosen the width of the active attractive patch as in the experiment of Hong et al.³ ($\Delta/\sigma = 0.05$). Given the very small width of the attractive wells, we expect the liquid phase to be metastable with respect to the corresponding solid one.^{17–19} Reduced densities $\rho^* = \rho\sigma^3$ and temperatures $T^* = k_B T/\epsilon$ will be employed throughout.

A. Technical details

The GEMC method is widely adopted as a standard method for calculating phase equilibria from molecular simulations. According to this method, the simulation is performed in two boxes (I and II) containing the coexisting phases. Equilibration in each phase is guaranteed by moving particles. Equality of pressures is satisfied in a statistical sense by expanding the volume of one of the boxes and contracting the volume of the other one, keeping the total volume constant. Chemical potentials are equalized by transferring particles from one box to the other one.

In the GEMC run we have on each step a probability $a_p/(a_p + a_v + a_s)$, $a_v/(a_p + a_v + a_s)$, and $a_s/(a_p + a_v + a_s)$ for a particle random displacement, a volume change, and a particle swap move between both boxes, respectively. We generally chose the relative weights $a_p = 1$, $a_v = 1/10$, and $a_s = 20$. To preserve the up-down fixed patch orientation, rotation of particles was not allowed. The maximum particle displacement was kept equal to $10^{-3}L^{(\gamma)}$ where $L^{(\gamma)}$ is the side of the (cubic) box $\gamma = \text{I, II}$. Regarding the volume changes, following Ref. 20 we performed a random walk in $\ln(V^{(\text{I})}/V^{(\text{II})})$, with $V^{(\gamma)}$ the volume of the box γ , choosing a maximum volume displacement of 1%. The volume move is computationally the most expensive one. This is because, after each volume move, it is necessary, in order to determine the next acceptance probability, to perform a full potential energy calculation since *all* the particle coordinates are rescaled by the factor associated with the enlargement or reduction of the boxes. However, this is not necessary for the other two moves since in those cases only the coordinates of a single particle change.

Both in the condensation and in the demixing problems, the Monte Carlo swap move consisted in moving a particle selected randomly in one box into the other box, so that the number of particles of each species in both boxes ($N_1^{(\text{I})}$, $N_2^{(\text{I})}$, $N_1^{(\text{II})}$, and $N_2^{(\text{II})}$) were fluctuating quantities. The only constraint was that the *total* number of particles was the same for both species, i.e., $N_1 \equiv N_1^{(\text{I})} + N_1^{(\text{II})} = N_2^{(\text{I})} + N_2^{(\text{II})} \equiv N_2 = N/2$. In the condensation problem we fixed the *global* density $\rho = N/(V^{(\text{I})} + V^{(\text{II})})$ (in all the cases we took $\rho^* = 0.3$, a value slightly below the expected critical density) and then varied the temperature T (below the critical temperature). The measured output quantities were the partial densities $\rho^{(\text{I})} = N^{(\text{I})}/V^{(\text{I})}$ and $\rho^{(\text{II})} = N^{(\text{II})}/V^{(\text{II})}$, where $N^{(\gamma)} = N_1^{(\gamma)} + N_2^{(\gamma)}$ is the total number of particles in box $\gamma = \text{I, II}$. Note that $(\rho^{(\text{II})} - \rho)/(\rho - \rho^{(\text{I})}) = V^{(\text{I})}/V^{(\text{II})}$. In contrast, in the demixing problem we fixed T (above the critical temperature) and varied ρ , the output observables being the local mole fractions $x_1^{(\text{I})} = N_1^{(\text{I})}/N^{(\text{I})}$ and $x_1^{(\text{II})} = N_1^{(\text{II})}/N^{(\text{II})}$. In this case, the lever rule is $(x_1^{(\text{II})} - \frac{1}{2})/(\frac{1}{2} - x_1^{(\text{I})}) = N^{(\text{I})}/N^{(\text{II})}$.

The total number of particles of each species was $N_1 = N_2 = 250$, what was checked to be sufficient for our

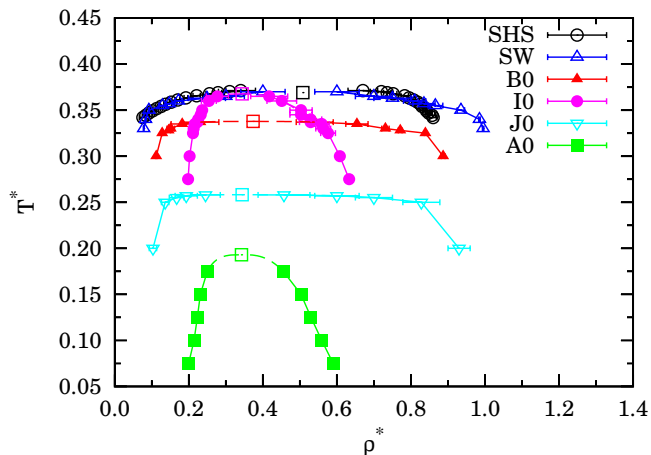


FIG. 3. Gas-liquid binodals for models SW, B0, I0, J0, and A0. The points indicated as SHS in the legend are grand canonical MC (GCMC) results taken from Ref. 22, where the actual one-component SHS model was studied. The remaining results are those obtained in this work from GEMC simulations. In each case, the solid line is a guide to the eye, while the dashed line is the result of the extrapolation to the critical point, which is represented by a square.

purposes. We used $50\text{--}100 \times 10^6$ MC steps for the equilibration (longer near the critical point) and $100\text{--}200 \times 10^6$ MC steps for the production.²¹

B. Gas-liquid coexistence

Results for the gas-liquid transition are depicted in Fig. 3 in the temperature-density plane. Some representative numerical values for models A0, B0, I0, and J0 are tabulated in Table II. In this case, one of the two simulation boxes ($I=g$) contains the gas phase and the other one ($II=l$) contains the liquid phase. Since $\rho_g < \rho < \rho_l$, the choice of the global density ρ establishes a natural bound as to how close to the critical point the measured binodal curve can be. In fact, $N^{(g)} \rightarrow 0$ if $\rho_l \rightarrow \rho$, while $N^{(g)} \rightarrow N$ if $\rho_g \rightarrow \rho$. As is apparent from the values of $N^{(g)}/N$ in Table II, the latter scenario seems to take place in our case $\rho^* = 0.3$.

Although not strictly enforced, we observed that $N_1^{(g)} \simeq N_2^{(g)}$ and $N_1^{(l)} \simeq N_2^{(l)}$ (so both boxes were practically equimolar) in models A0, B0, and J0. On the other hand, in the case of model I0 the final equilibrium state was non-equimolar (despite the fact that, as said before, $N_1 = N_2$ globally), the low-density box having a more disparate composition than the high-density box. The mole fraction values are shown in Table III. Thus, in contrast to models A0, B0, and J0, the GEMC simulations at fixed temperature and global density $\rho^* = 0.3$ spontaneously drove the system I0 into two coexisting boxes differing both in density and composition. This *spontaneous demixing* phenomenon means that in model I0 the

equimolar binodal curve must be metastable with respect to demixing and so it was not observed in our simulations. It is important to remark that, while the equimolar binodal must be robust with respect to changes in the global density ρ (except for the bound $\rho_g < \rho < \rho_l$ mentioned above), the non-equimolar binodal depends on the value of ρ .

In addition to cases SW, B0, I0, J0, and A0, we have also included in Fig. 3, for completeness, numerical results obtained by Miller and Frenkel²² on the one-component Baxter’s sticky-hard-sphere (SHS) model.²³ As expected, they agree quite well with our short-range SW results, the only qualitative difference being a liquid branch at slightly larger densities.

In order to determine the critical point (T_c^*, ρ_c^*) we empirically extrapolated the GEMC binodals using the law of rectilinear “diameters”,²⁴ $\frac{1}{2}(\rho_g^* + \rho_l^*) = \rho_c^* + A|T^* - T_c^*|$, and the Wegner expansion^{24,25} for the width of the coexistence curve, $\rho_l^* - \rho_g^* = B|T^* - T_c^*|^{\beta_I}$. The critical coordinates (T_c^*, ρ_c^*) and the coefficients A and B are taken as fitting parameters. The four points corresponding to the two highest temperatures were used for the extrapolation in each case. We remark that our data do not extend sufficiently close to the critical region to allow for quantitative estimates of critical exponents and non-universal quantities. However, assuming that the models belong to the three-dimensional Ising universality class, we chose $\beta_I = 0.325$. The numerical values obtained by this extrapolation procedure will be presented in Table V below.

The decrease in the critical temperatures and densities in going from the one-component SW fluid to model B0 and then to model A0 is strongly reminiscent of an analogous trend present in the unconstrained one-patch Kern–Frenkel model upon decrease of the coverage.²⁶

It is interesting to remark that, even though the influence of attraction in model A0 is strongly inhibited by the up-down constrained orientation ($\epsilon_{ij} = \epsilon \delta_{i1} \delta_{j2}$), this model exhibits a gas-liquid transition. This surprising result was preliminarily supported by canonical NVT MC simulations in Ref. 12, but now it is confirmed by the new and more appropriate GEMC simulations presented in this paper. Given the patch geometry and interactions in model A0, one might expect the formation of a lamellar-like liquid phase (approximately) made of alternating layers (up-down-up-down-...) of particles with the same orientation. This scenario is confirmed by snapshots of the liquid-phase box, as illustrated by Fig. 4.

The Kern–Frenkel analogy is not applicable to the isotropic models I0 and J0. Model J0 presents a critical point intermediate between those of models B0 and A0, as expected. However, while the decrease in the total average attractive strength is certainly one of the main mechanisms dictating the location of the gas-liquid coexistence curves, it cannot be the only discriminating factor, as shown by the results for the isotropic model I0, where the critical temperature is higher and the binodal curve is narrower than that corresponding to the

TABLE II. Gas-liquid coexistence properties for models A0, B0, I0, and J0, as obtained from our GEMC simulations. T^* is the reduced temperature, ρ_γ^* is the reduced density of the gas ($\gamma = g$) and liquid ($\gamma = l$) phases, $N^{(g)}$ is the average number of particles in the gas box, and $U_{\text{ex}}^{(\gamma)}/N^{(\gamma)}$ is the excess internal energy per particle in box γ .

Model	T^*	ρ_g^*	ρ_l^*	$N^{(g)}/N$	$-U_{\text{ex}}^{(g)}/\epsilon N^{(g)}$	$-U_{\text{ex}}^{(l)}/\epsilon N^{(l)}$
A0	0.075	0.1994(6)	0.590(1)	0.493(2)	1.69(1)	1.796(7)
	0.1	0.214(2)	0.559(5)	0.535(4)	1.785(4)	1.780(8)
	0.125	0.223(1)	0.530(6)	0.556(3)	1.63(9)	1.71(5)
	0.15	0.231(1)	0.503(4)	0.574(4)	1.60(1)	1.78(1)
	0.175	0.250(2)	0.455(8)	0.630(6)	1.42(1)	1.632(9)
B0	0.3	0.112(2)	0.887(5)	0.284(5)	1.6(1)	3.27(1)
	0.325	0.128(1)	0.839(3)	0.324(3)	0.761(1)	3.239(7)
	0.328	0.145(5)	0.771(5)	0.363(9)	0.88(2)	2.99(1)
	0.33	0.15(1)	0.73(1)	0.380(1)	0.95(1)	3.016(9)
	0.335	0.18(3)	0.65(3)	0.45(1)	1.0(7)	2.83(2)
	0.337	0.23(5)	0.54(5)	0.59(1)	1.273(4)	2.36(4)
I0	0.3	0.202(3)	0.61(1)	0.5146(7)	2.48(6)	3.04(1)
	0.325	0.211(5)	0.58(2)	0.5371(6)	1.76(4)	2.765(8)
	0.35	0.24(1)	0.50(3)	0.612(3)	1.24(3)	2.30(1)
	0.36	0.25(2)	0.45(4)	0.657(5)	1.01(1)	1.85(5)
	0.365	0.28(3)	0.42(5)	0.71(1)	0.96(2)	1.6(1)
J0	0.2	0.10(1)	0.93(3)	0.249(5)	1.67(2)	2.48(3)
	0.25	0.14(1)	0.83(5)	0.34(1)	0.82(2)	2.25(3)
	0.255	0.17(2)	0.70(5)	0.433(9)	0.90(2)	1.99(2)
	0.257	0.19(3)	0.60(6)	0.62(6)	1.10(7)	1.5(2)

TABLE III. Mole fractions in the gas and liquid boxes in model I0 at different temperatures and with a global density $\rho^* = 0.3$. For the gas and liquid densities, see Table II. Because of the symmetry under label exchange $1 \leftrightarrow 2$, we have adopted the criterion $x_1^{(g)} \leq x_2^{(g)}$ without loss of generality.

T^*	$x_1^{(g)}$	$x_1^{(l)}$
0.3	0.03(1)	0.992(6)
0.325	0.09(2)	0.98(1)
0.35	0.18(3)	0.955(15)
0.36	0.26(3)	0.93(3)
0.365	0.34(3)	0.89(4)

anisotropic model B0. This may be due to the fact that, as said before, the binodal curve in model I0 is not equimolar and this lack of equimolarity is expected to extend to the critical point, as can be guessed from the trends observed in Table III. In other words, two demixed phases can be made to coexist at a higher temperature and with a smaller density difference than two mixed phases.

C. Demixing transition

The bi-component nature of the systems raises the question of a possible demixing transition in which a rich-1 phase coexists with a rich-2 phase at a given temper-

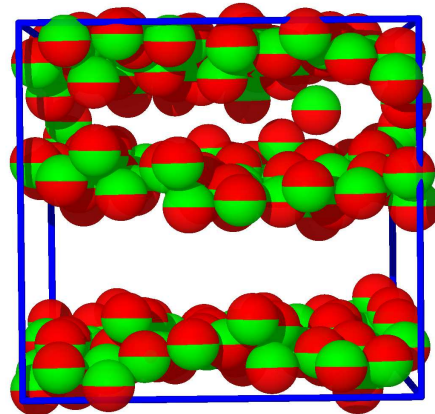


FIG. 4. Snapshot of the liquid-phase box in model A0 at $T^* = 0.15$.

ature T , provided the density is larger than a certain critical consolute density $\rho_{cc}(T)$. The points $\rho_{cc}(T)$ or, reciprocally, $T_{cc}(\rho)$ define the so-called λ -line.²⁷ The interplay between the gas-liquid and demixing transitions is a very interesting issue and was discussed in a general framework by Wilding et al.²⁸

Since all the spheres have the same size, a neces-

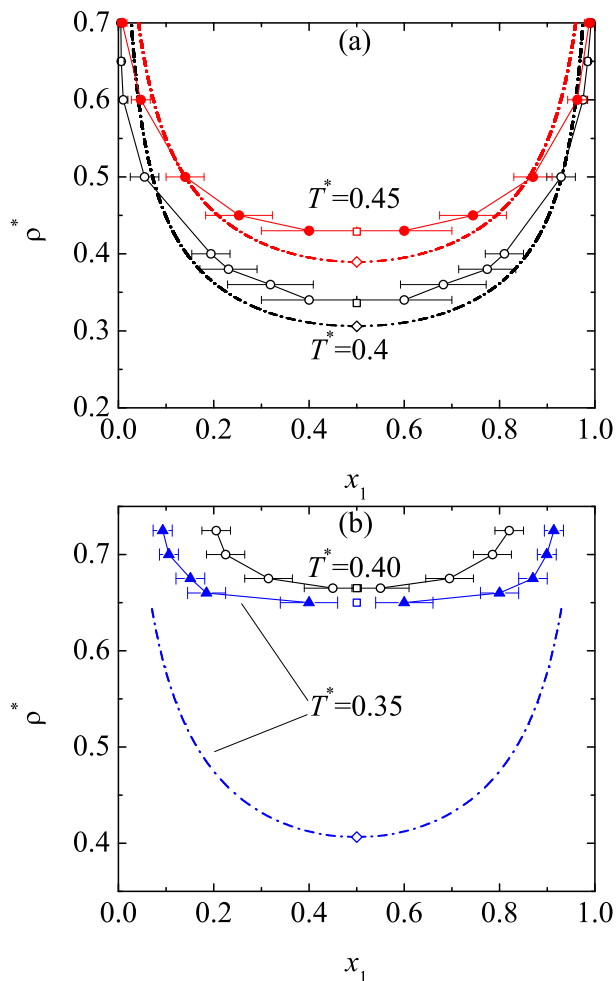


FIG. 5. Demixing curves for models (a) I0 and (b) B0 at two temperatures, as obtained from GEMC simulations, in the density-mole fraction plane. In each case, the solid line is a guide to the eye, while the critical consolute point is represented by a square. For model I0 we found $\rho_{cc}^*(T^* = 0.4) = 0.336$ and $\rho_{cc}^*(T^* = 0.45) = 0.429$; for model B0 the results are $\rho_{cc}^*(T^* = 0.35) = 0.650$ and $\rho_{cc}^*(T^* = 0.4) = 0.665$. The dashed-dotted lines are the theoretical predictions (see Sec. IV C).

sary condition for demixing in the case of *isotropic* potentials is that the like attractions must be sufficiently stronger than the unlike attractions.^{28,29} Assuming the validity of this condition to anisotropic potentials and making a simple estimate based on the virial expansion, one finds that demixing requires the coefficient of x_1x_2 in the second virial coefficient to be positive, i.e., $2e^{\epsilon_{11}/k_B T} > e^{\epsilon_{12}/k_B T} + e^{\epsilon_{21}/k_B T}$. While this demixing criterion is only approximate, it suggests that, out of the five models considered, only models B0 and I0 are expected to display demixing transitions. As a matter of fact, we have already discussed the spontaneous demixing phenomenon taking place in model I0 when a low-density phase and a high-density phase are in mutual equilibrium. In this

TABLE IV. Demixing coexistence properties for models I0 and B0, as obtained from our GEMC simulations. T^* is the reduced temperature, ρ^* is the reduced density, and $x_1^{(\gamma)}$ is the mole fraction of species 1 in each one of the two coexisting phases $\gamma = \text{I, II}$.

Model	T^*	ρ^*	$x_1^{(\text{I})}$	$x_1^{(\text{II})}$
I0	0.4	0.7	0.005(5)	0.992(5)
		0.65	0.006(6)	0.985(6)
		0.6	0.01(1)	0.97(1)
		0.5	0.05(3)	0.93(3)
		0.4	0.19(4)	0.81(4)
		0.38	0.23(6)	0.77(6)
		0.36	0.32(9)	0.68(9)
		0.34	0.4(1)	0.6(1)
	0.45	0.7	0.01(1)	0.99(1)
		0.6	0.05(2)	0.96(2)
		0.5	0.14(4)	0.87(4)
		0.45	0.25(7)	0.74(7)
		0.43	0.4(1)	0.6(1)
B0	0.35	0.725	0.09(2)	0.91(2)
		0.7	0.11(2)	0.90(2)
		0.675	0.15(3)	0.87(3)
		0.66	0.18(4)	0.80(4)
		0.65	0.40(6)	0.60(6)
	0.4	0.725	0.20(3)	0.82(3)
		0.7	0.22(4)	0.78(4)
		0.675	0.31(5)	0.69(5)
		0.665	0.45(6)	0.55(6)

section, however, we are interested in the segregation of the system, at a given T and for $\rho > \rho_{cc}(T)$, into a rich-2 phase I with $x_1^{(\text{I})} = x_d(\rho) < \frac{1}{2}$ and a *symmetric* rich-1 phase II with $x_1^{(\text{II})} = 1 - x_d(\rho) > \frac{1}{2}$, both phases at the *same* density.

Our GEMC simulation results are presented in Fig. 5 and Table IV. We observe that, as expected, $x_1^{(\text{I})} = 1 - x_1^{(\text{II})}$ within statistical fluctuations. We have also checked that $\rho^{(\text{I})} \simeq \rho^{(\text{II})}$, even though this equality is not artificially enforced in the simulations. Such equality is also equivalent to $\rho^{(\text{I})} \simeq \rho$ and we checked that it was satisfied within a standard deviation of $0.02\sigma^{-3}$ in all cases considered in Table IV. To obtain the critical consolute density ρ_{cc}^* for each temperature, we extrapolated the data again according to the Ising scaling relation $\frac{1}{2} - x_d(\rho) = C(\rho - \rho_{cc})^{\beta_I}$.

It is interesting to note that just the absence of attraction when a particle of species 2 is below a particle of species 1 ($\epsilon_{21} = 0$) in model B0 is sufficient to drive a demixing transition. However, as expected, at a common temperature (see $T^* = 0.4$ in Fig. 5), demixing requires higher densities in model B0 than in model I0.

As said above, the interplay of condensation and demixing is an interesting problem by itself.^{28,30} Three alternative scenarios are in principle possible for the in-

tersection of the λ -line and the binodal curve: a critical end point, a triple point, or a tricritical point.²⁸ Elucidation of these scenarios would require grand canonical simulations (rather than GEMC simulations), what is beyond the scope of this paper.

IV. SIMPLE ANALYTICAL THEORIES

Let us now compare the above numerical results with simple theoretical predictions. The solution of integral equation theories for anisotropic interactions and/or multicomponent systems requires formidable numerical efforts, with the absence of explicit expressions often hampering physical insight. Here we want to deal with simple, purely analytical theories that yet include the basic ingredients of the models.

First, we take advantage of the short-range of the attractive well ($\Delta/\sigma = 0.05$) to map the different SW interactions into SHS interactions parameterized by the ‘‘stickiness’’ parameters¹²

$$t_{ij} \equiv \frac{1}{12\tau_{ij}} \equiv \frac{\Delta}{\sigma} \left(1 + \frac{\Delta}{\sigma} + \frac{\Delta^2}{3\sigma^2} \right) \left(e^{\epsilon_{ij}/k_B T} - 1 \right), \quad (3)$$

which combine the energy and length scales. This mapping preserves the exact second virial coefficient of the genuine SW systems, namely

$$\frac{B_2}{B_2^{\text{HS}}} = 1 - 3t_{11} + 3x_1x_2(2t_{11} - t_{12} - t_{21}), \quad (4)$$

where $B_2^{\text{HS}} = 2\pi\sigma^3/3$ is the HS coefficient. The exact expression of the third virial coefficient B_3 in the SHS limit for arbitrary t_{ij} is¹²

$$\begin{aligned} \frac{B_3}{B_3^{\text{HS}}} = & 1 - 6t_{11} + \frac{72}{5}t_{11}^2 - \frac{48}{5}t_{11}^3 - \frac{6}{5}x_1x_2 \left[(12t_{11} - 5) \right. \\ & \times (2t_{11} - t_{12} - t_{21}) - 8t_{11}(t_{11}^2 - t_{12}t_{21}) \\ & \left. - 2(4t_{11} - 3)(2t_{11}^2 - t_{12}^2 - t_{21}^2) + 2\alpha(t_{12} - t_{21})^2 \right], \end{aligned} \quad (5)$$

where $B_3^{\text{HS}} = 5\pi^2\sigma^6/18$ and

$$\alpha \equiv \frac{3\sqrt{3}}{\pi} - 1. \quad (6)$$

A. Equations of state

One advantage of the SW \rightarrow SHS mapping is that the Percus–Yevick (PY) integral equation is exactly solvable for SHS mixtures with *isotropic* interactions ($t_{12} = t_{21}$).^{31,32} In principle, that solution can be applied to the models SW, I0, and J0 represented in Fig. 2. On the other hand, if $t_{11} \neq 0$ (models SW and I0), the PY solutions are related to algebraic equations of second (SW)

or fourth (I0) degrees, what creates the problem of disappearance of the physical solution for large enough densities or stickiness. In particular, we have observed that the breakdown of the solution preempts the existence of a critical point in model I0. However, in the case of model J0 ($t_{11} = 0$, $t_{12} = t_{21} = t$), the PY solution reduces to a *linear* equation whose solution is straightforward. Following the virial (v) and the energy (u) routes, the respective expressions for the compressibility factor $Z \equiv P/\rho k_B T$ (where P is the pressure) have the form

$$Z_v(\eta, t, x_1) = Z_v^{\text{HS}}(\eta) - x_1x_2Z_v^{(1)}(\eta, t) - x_1^2x_2^2Z_v^{(2)}(\eta, t), \quad (7)$$

$$Z_u(\eta, t, x_1) = Z_u^{\text{HS}}(\eta) - x_1x_2Z_u^{(1)}(\eta, t), \quad (8)$$

where $\eta = \pi\rho^*/6$ is the packing fraction,

$$Z_v^{\text{HS}}(\eta) = \frac{1 + 2\eta + 3\eta^2}{(1 - \eta)^2} \quad (9)$$

is the HS compressibility factor derived from the PY equation via the virial route, Z_u^{HS} is an indeterminate integration constant, and the explicit expressions for $Z_v^{(1)}$, $Z_v^{(2)}$, and $Z_u^{(1)}$ are

$$\begin{aligned} Z_v^{(1)}(\eta, t) = & \frac{24\eta t}{(1 - \eta + 6\eta t)^2} \left[\frac{1 + 2\eta}{1 - \eta} + 3\eta t \frac{2 + 2\eta - 5\eta^2/2}{(1 - \eta)^2} \right. \\ & \left. + 6\eta^2 t^2 \frac{2 - 4\eta - 7\eta^2}{(1 - \eta)^3} \right], \end{aligned} \quad (10)$$

$$\begin{aligned} Z_v^{(2)}(\eta, t) = & \frac{288\eta^3 t^2 (2 + \eta)}{(1 - \eta + 6\eta t)^3} \left[\frac{1}{1 - \eta} - t \frac{2 - 11\eta}{(1 - \eta)^2} \right. \\ & \left. + t^2 \frac{2 - 10\eta + 61\eta^2/2}{(1 - \eta)^3} \right], \end{aligned} \quad (11)$$

$$Z_u^{(1)}(\eta, t) = \frac{6\eta}{(1 - \eta)^2} \left[\frac{2t(2 + \eta)}{1 - \eta + 6\eta t} + \ln \frac{1 - \eta + 6\eta t}{1 - \eta} \right]. \quad (12)$$

To the best of our knowledge, this extremely simple solution of the PY integral equation for a model of SHS mixtures had not been unveiled before.

As apparent from Fig. 2, model A0 is a close relative of model J0. However, the fact that $\epsilon_{12} \neq \epsilon_{21} = 0$ (or $t_{12} \neq t_{21} = 0$) makes the interaction anisotropic and prevents the PY equation from being exactly solvable in this case. On the other hand, we have recently proposed¹² a simple rational-function approximation (RFA) that applies to models with $t_{12} \neq t_{21}$ and reduces to the PY solution in the case of isotropic models ($t_{12} = t_{21}$). The RFA solution for model A0 yields once more a linear equation. The virial and energy equations of state are again of the forms (7) and (8), respectively, with expressions for $Z_v^{(1)}$, $Z_v^{(2)}$, and $Z_u^{(1)}$ given by

$$Z_v^{(1)}(\eta, t) = \frac{12\eta t}{1 - \eta + 6\eta t} \left[\frac{1 + 2\eta}{(1 - \eta)^2} + 2\eta t \frac{1 - 2\eta - 7\eta^2/2}{(1 - \eta)^3} \right], \quad (13)$$

$$Z_v^{(2)}(\eta, t) = \frac{72\eta^3 t^2 (2 + \eta)}{(1 - \eta)^3 (1 - \eta + 6\eta t)}, \quad (14)$$

$$Z_u^{(1)}(\eta, t) = \frac{3\eta}{(1 - \eta)^2} \left[\frac{2t(2 + \eta)}{1 - \eta + 6\eta t} + \ln \frac{1 - \eta + 6\eta t}{1 - \eta} \right]. \quad (15)$$

In the RFA solution for model A0 the exact third virial coefficient (5) is recovered by the interpolation formula

$$\begin{aligned} Z &= Z_{\text{CS}}^{\text{HS}} + \alpha (Z_v - Z_v^{\text{HS}}) + (1 - \alpha) (Z_u - Z_u^{\text{HS}}) \\ &= Z_{\text{CS}}^{\text{HS}} - x_1 x_2 \left[\alpha Z_v^{(1)} + (1 - \alpha) Z_u^{(1)} \right] - x_1^2 x_2^2 \alpha Z_v^{(2)}, \end{aligned} \quad (16)$$

where

$$Z_{\text{CS}}^{\text{HS}}(\eta) = \frac{1 + \eta + \eta^2 - \eta^3}{(1 - \eta)^3} \quad (17)$$

is the HS Carnahan–Starling compressibility factor and the interpolation weight α is given by Eq. (6). By consistency, Eq. (16) will also be employed in the PY solution of model J0.

In the cases of models with $\epsilon_{11} \neq 0$ (i.e., SW, B0, and I0), the PY and RFA theories fail to have physical solutions in regions of the temperature-density plane overlapping with the gas-liquid transition. In order to circumvent this problem, we adopt here a simple perturbative approach:

$$Z = Z^{\text{ref}} + (B_2 - B_2^{\text{ref}}) \rho + (B_3 - B_3^{\text{ref}}) \rho^2, \quad (18)$$

where Z^{ref} is the compressibility factor of a reference model and B_2^{ref} and B_3^{ref} are the associated virial coefficients. As a natural choice (see Fig. 2), we take the models J0, A0, and HS (which lie on the plane $\epsilon_{11}/\epsilon = 0$) as reference systems for the models SW, B0, and I0 (which lie on the plane $\epsilon_{11}/\epsilon = 1$), respectively. More specifically,

$$Z^{\text{SW}} = Z^{\text{J0}} + (B_2^{\text{SW}} - B_2^{\text{J0}}) \rho + (B_3^{\text{SW}} - B_3^{\text{J0}}) \rho^2, \quad (19)$$

$$Z^{\text{B0}} = Z^{\text{A0}} + (B_2^{\text{B0}} - B_2^{\text{A0}}) \rho + (B_3^{\text{B0}} - B_3^{\text{A0}}) \rho^2, \quad (20)$$

$$Z^{\text{I0}} = Z_{\text{CS}}^{\text{HS}} + (B_2^{\text{I0}} - B_2^{\text{HS}}) \rho + (B_3^{\text{I0}} - B_3^{\text{HS}}) \rho^2. \quad (21)$$

Here, Z^{J0} and Z^{A0} are given by Eq. (16) (with the corresponding expressions of $Z_v^{(1)}$, $Z_v^{(2)}$, and $Z_u^{(1)}$) and the virial coefficients are obtained in each case from Eqs. (4) and (5) with the appropriate values of t_{11} , t_{12} , and t_{21} .

From the explicit knowledge of $Z(\eta, t, x_1)$, standard thermodynamic relations allow one to obtain the free energy per particle $a(\eta, t, x_1)$ and the chemical potentials $\mu_i(\eta, t, x_1)$ as

$$\begin{aligned} \beta a(\eta, t, x_1) &= \int_0^\eta d\eta' \frac{Z(\eta', t, x_1) - 1}{\eta'} + x_1 \ln(x_1 \eta) \\ &\quad + (1 - x_1) \ln[(1 - x_1)\eta] + \text{const}, \end{aligned} \quad (22)$$

TABLE V. Comparison between the critical points measured in simulations with those obtained from theoretical approaches.

Method	SW	B0	I0	J0	A0
		T_c^*			
Simulation	0.369 ^a	0.338 ^b	0.368 ^b	0.258 ^b	0.193 ^b
Our theory	0.377	0.341	0.331	0.278	0.214
Noro–Frenkel	0.369	0.335	0.297	0.297	0.247
		ρ_c^*			
Simulation	0.508 ^a	0.373 ^b	0.344 ^b	0.344 ^b	0.342 ^b
Our theory	0.356	0.330	0.366	0.376	0.359

^a GCMC results for the one-component SHS fluid From Ref. 22

^b Our GEMC simulation results

$$\begin{aligned} \beta \mu_1(\eta, t, x_1) &= \beta a(\eta, t, x_1) + Z(\eta, t, x_1) \\ &\quad + (1 - x_1) \frac{\partial \beta a(\eta, t, x_1)}{\partial x_1}, \end{aligned} \quad (23)$$

$$\mu_2(\eta, t, x_1) = \mu_1(\eta, t, 1 - x_1), \quad (24)$$

where $\beta \equiv 1/k_B T$.

B. Gas-liquid coexistence

The critical point (η_c, t_c) of the gas-liquid transition is obtained from the well-known condition that the critical isotherm in the pressure-density plane presents an inflection point with horizontal slope at the critical density.³³ In terms of the compressibility factor Z , this implies

$$\left. \frac{\partial [\eta Z(\eta, t_c, 1/2)]}{\partial \eta} \right|_{\eta=\eta_c} = \left. \frac{\partial^2 [\eta Z(\eta, t_c, 1/2)]}{\partial \eta^2} \right|_{\eta=\eta_c} = 0, \quad (25)$$

where equimolarity ($x_1 = \frac{1}{2}$) has been assumed. For temperatures below the critical temperature (i.e., $t > t_c$) the packing fractions η_g and η_l of the gas and liquid coexisting phases are obtained from the conditions of equal pressure (mechanical equilibrium) and equal chemical potential (chemical equilibrium),³³ i.e.

$$\eta_g Z(\eta_g, t, 1/2) = \eta_l Z(\eta_l, t, 1/2), \quad (26)$$

$$\mu_1(\eta_g, t, 1/2) = \mu_1(\eta_l, t, 1/2). \quad (27)$$

In order to make contact with the GEMC results, the theoretical values of t_c have been mapped onto those of T_c^* by inverting Eq. (3), namely

$$\frac{1}{T^*} = \ln \left[1 + \frac{t}{(\Delta/\sigma)(1 + \Delta/\sigma + \Delta^2/3\sigma^2)} \right] \quad (28)$$

with $\Delta/\sigma = 0.05$.

Table V compares the critical points obtained in simulations for the one-component SW fluid (in the SHS limit) and for models B0, I0, J0, and A0 (see Fig. 2)

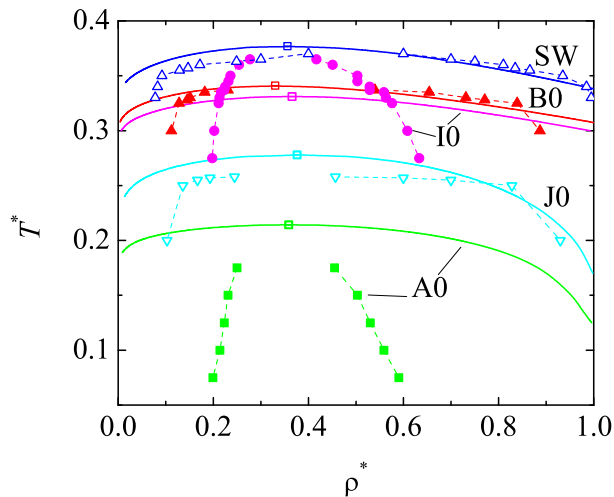


FIG. 6. Gas-liquid binodals for models SW, A0, B0, I0, and J0, as obtained from our theoretical method (solid lines). The critical points are represented by open squares. The symbols joined by dashed lines correspond to our GEMC data (see Fig. 3).

with those stemming from our simple theoretical method. Results from the Noro–Frenkel (NF) corresponding-state criterion,³⁴ according to which $B_2/B_2^{\text{HS}} = -1.21$ at the critical temperature, are also included. We observe that, despite its simplicity and the lack of fitting parameters, our fully analytical theory predicts quite well the location of the critical point, especially in the case of T_c^* . It improves the estimates obtained from the NF criterion, except in the SW case, where, by construction, the NF rule gives the correct value. In what concerns the gas-liquid binodals, Fig. 6 shows that the theoretical curves agree fairly well with the GEMC data, except in the cases of models I0 and A0, where the theoretical curves are much flatter than the simulation ones. The lack of agreement with the binodal curve of model I0 can be partially due to the fact that in the theoretical treatment the two co-existing phases are supposed to be equimolar, while this is not the case in the actual simulations (see Table III).

C. Demixing transition

In the case of the demixing transition, the critical consolute density η_{cc} at a given temperature is obtained from

$$\left. \frac{\partial^2 a(\eta_{cc}, t, x_1)}{\partial x_1^2} \right|_{x_1=\frac{1}{2}} = 0. \quad (29)$$

For $\eta > \eta_{cc}$, the demixing mole fraction $x_1 = x_d(\eta)$ is the solution to

$$\mu_1(\eta, t, x_d) = \mu_1(\eta, t, 1 - x_d). \quad (30)$$

In terms of the compressibility factor Z , Eqs. (29) and (30) can be rewritten as

$$\int_0^{\eta_{cc}} d\eta \frac{\partial^2 Z(\eta, t, x_1)/\partial x_1^2|_{x_1=\frac{1}{2}}}{\eta} = -4, \quad (31)$$

$$\int_0^\eta d\eta' \frac{\partial Z(\eta', t, x_d)/\partial x_d}{\eta'} = \ln \frac{1 - x_d}{x_d}, \quad (32)$$

respectively.

The perturbative approximations for models I0 and B0 succeed in predicting demixing transitions, even though their respective reference systems (HS and A0) do not demix. In the case of model I0, the critical consolute densities are $\rho_{cc}^*(T^* = 0.4) = 0.306$ and $\rho_{cc}^*(T^* = 0.45) = 0.390$, which are about 9% lower than the values obtained in our GEMC simulations. In the case of model B0, our simple theory predicts a critical consolute point only if $t > 0.7667$, i.e., if $T^* < 0.364$, so no demixing is predicted at $T^* = 0.4$, in contrast to the results of the simulations. At $T^* = 0.35$ the theoretical prediction is $\rho_{cc}^* = 0.406$, a value about 39% smaller than the GEMC one. The theoretical demixing curves at $T^* = 0.4$ and $T^* = 0.45$ for model I0 and at $T^* = 0.35$ for model B0 are compared with the GEMC results in Fig. 5. We can observe a fairly good agreement in the case of model I0, but not for model B0. In the latter case, the theoretical curve spans a density range comparable to that of model I0, while simulations show a much flatter demixing curve.

V. CONCLUDING REMARKS

In conclusion, we have proposed a novel class of binary-mixture Janus fluids with up-down constrained orientations. The class encompasses, as particular cases, the conventional one-component SW fluid, mixtures with isotropic attractive interactions only between like particles (model I0) or unlike particles (model J0), and genuine Janus fluids with anisotropic interactions and different patch-patch affinities (models A0 and B0). Both GEMC numerical simulations and simple theoretical approximations have been employed to analyze the gas-liquid transition under *global* equimolar conditions for the five models and the demixing transition for the two models (I0 and B0) where the attraction between like particles is stronger than between unlike ones. The theoretical analysis employed a mapping onto SHS interactions, that were then studied by means of the PY theory (model J0), the RFA (model A0), and low-density virial corrections (models SW, I0, and B0), with semi-quantitative agreement with numerical simulations.

Interestingly, the presence of attraction in only one out of the four possible patch-patch interactions (model A0) turns out to be enough to make the gas-liquid transition possible. Reciprocally, the lack of attraction in only one of the two possible patch-patch interactions between unlike particles (model B0) is enough to produce a demixing

transition. Except in model I0, the coexisting gas and liquid phases have an equimolar composition. As the average attraction is gradually decreased, the gas-liquid critical point shifts to lower temperatures (except for an interesting inversion of tendency observed when going from the isotropic model I0 to the anisotropic model B0) and lower densities. Moreover, the coexistence region progressively shrinks, in analogy with what is observed in the unconstrained one-component Janus fluid^{35,36} and in the empty liquid scenario.³⁷ On the other hand, the imposed constraint in the orientation of the attractive patches does not allow for the formation of those inert clusters^{38–40} which in the original Janus fluid are responsible for a re-entrant gas branch.^{26,38,41}

ACKNOWLEDGMENTS

The authors are grateful to J.-P. Hansen for useful suggestions. R.F. acknowledges the use of the PLX computational facility of CINECA through the ISCRA call. A.G. acknowledges funding from PRIN-COFIN2010-2011 (contract 2010LKE4CC). The research of M.A.G.M. and A.S. has been supported by the Spanish government through Grant No. FIS2010-16587 and by the Junta de Extremadura (Spain) through Grant No. GR101583, partially financed by FEDER funds. M.A.G.M. is also grateful to the Junta de Extremadura (Spain) for the predoctoral fellowship PD1010.

¹S. C. Glotzer and M. J. Solomon, *Nature Mater.* **6**, 557 (2007).

²A. Walther and H. E. Müller, *Soft Matter* **4**, 663 (2008).

³L. Hong, A. Cacciuto, E. Luijten, and S. Granick, *Langmuir* **24**, 621 (2008).

⁴A. B. Pawar and I. Kretzschmar, *Macromol. Rapid Comm.* **31**, 150 (2010).

⁵A. Walther and A. H. E. Müller, *Chem. Rev.* **113**, 5194 (2013).

⁶E. Bianchi, R. Blaak, and C. N. Likos, *Phys. Chem. Chem. Phys.* **13**, 6397 (2011).

⁷S. Jiang and S. Granick, eds., *Janus Particle Synthesis, Self-Assembly and Applications* (Royal Society of Chemistry, London, 2012).

⁸R. Fantoni, *The Janus Fluid: A Theoretical Perspective* (Springer, New York, 2013).

⁹S. Gangwal, *Directed Assembly and Manipulation of Anisotropic Colloidal Particles by External Fields* (ProQuest, UMI Dissertation Publishing, Ann Arbor, Michigan, 2011).

¹⁰S. Gangwal, A. Pawar, I. Kretzschmar, and O. D. Velev, *Soft Matter* **6**, 1413 (2010).

¹¹N. Kern and D. Frenkel, *J. Chem. Phys.* **118**, 9882 (2003).

¹²M. A. G. Maestre, R. Fantoni, A. Giacometti, and A. Santos, *J. Chem. Phys.* **138**, 094904 (2013).

¹³E. Zaccarelli, G. Foffi, P. Tartaglia, F. Sciortino, and K. Dawson, *Prog. Colloid Polym. Sci.* **115**, 371 (2000).

¹⁴A. Z. Panagiotopoulos, *Mol. Phys.* **61**, 813 (1987).

¹⁵B. Smit, P. de Smedt, and D. Frenkel, *Mol. Phys.* **68**, 931 (1989).

¹⁶B. Smit and D. Frenkel, *Mol. Phys.* **68**, 951 (1989).

¹⁷H. Liu, S. Garde, and S. Kumar, *J. Chem. Phys.* **123**, 174505 (2005).

¹⁸M. A. Miller and D. Frenkel, *Phys. Rev. Lett.* **90**, 135702 (2003).

¹⁹T. Vissers, Z. Preisler, F. Smalenburg, M. Dijkstra, and F. Sciortino, *J. Chem. Phys.* **138**, 164505 (2013).

²⁰D. Frenkel and B. Smit, *Understanding Molecular Simulation: From Algorithms to Applications* (Academic Press, San Diego, 2002), 2nd ed.

²¹The GEMC code took ≈ 55 seconds of CPU time for one million steps of a system of size $N = 100$ on the IBM iDataPlex DX360M3 Cluster (2.40GHz).

²²M. A. Miller and D. Frenkel, *J. Chem. Phys.* **121**, 535 (2004).

²³R. J. Baxter, *J. Chem. Phys.* **49**, 2770 (1968).

²⁴J. V. Sengers and J. M. H. Levelt-Sengers, in *Progress in Liquid Physics*, edited by C. A. Croxton (Wiley, Chichester, 1978), chap. 4.

²⁵F. Wegner, *Phys. Rev. B* **5**, 4529 (1972).

²⁶F. Sciortino, A. Giacometti, and G. Pastore, *Phys. Chem. Chem. Phys.* **12**, 11869 (2010).

²⁷N. B. Wilding, *Phys. Rev. E* **52**, 602 (1995).

²⁸N. Wilding, F. Schmid, and P. Nielaba, *Phys. Rev. E* **58**, 2201 (1998).

²⁹R. Fantoni, D. Gazzillo, and A. Giacometti, *Phys. Rev. E* **72**, 011503 (2005).

³⁰W. M. Jacobs and D. Frenkel, *J. Chem. Phys.* **139**, 024108 (2013).

³¹J. W. Perram and E. R. Smith, *Chem. Phys. Lett.* **35**, 138 (1975).

³²B. Barbooy, *Chem. Phys.* **11**, 357 (1975).

³³J.-P. Hansen and I. R. McDonald, *Theory of Simple Liquids* (Academic Press, London, 2006).

³⁴M. G. Noro and D. Frenkel, *J. Chem. Phys.* **113**, 2941 (2000).

³⁵R. Fantoni, D. Gazzillo, A. Giacometti, M. A. Miller, and G. Pastore, *J. Chem. Phys.* **127**, 234507 (2007).

³⁶C. Gögelein, F. Romano, F. Sciortino, and A. Giacometti, *J. Chem. Phys.* **136**, 094512 (2012).

³⁷E. Bianchi, J. Largo, E. Zaccarelli, and F. Sciortino, *Phys. Rev. Lett.* **97**, 168301 (2006).

³⁸F. Sciortino, A. Giacometti, and G. Pastore, *Phys. Rev. Lett.* **103**, 237801 (2009).

³⁹R. Fantoni, A. Giacometti, F. Sciortino, and G. Pastore, *Soft Matter* **7**, 2419 (2011).

⁴⁰R. Fantoni, *Eur. Phys. J. B* **85**, 108 (2012).

⁴¹A. Reinhardt, A. J. Williamson, J. P. K. Doye, J. Carrete, L. M. Varela, and A. A. Louis, *J. Chem. Phys.* **134**, 104905 (2011).